BNL-211500-2019-JAAM

In Situ Study of ABC Triblock Terpolymer Self-Assembly under Solvent Vapor Annealing

S. Lee, K. Yager

To be published in "Macromolecules"

February 2019

Center for Functional Nanomaterials

Brookhaven National Laboratory

U.S. Department of Energy

USDOE Office of Science (SC), Basic Energy Sciences (BES) (SC-22)

Notice: This manuscript has been authored by employees of Brookhaven Science Associates, LLC under Contract No. DE-SC0012704 with the U.S. Department of Energy. The publisher by accepting the manuscript for publication acknowledges that the United States Government retains a non-exclusive, paid-up, irrevocable, world-wide license to publish or reproduce the published form of this manuscript, or allow others to do so, for United States Government purposes.

DISCLAIMER

This report was prepared as an account of work sponsored by an agency of the United States Government. Neither the United States Government nor any agency thereof, nor any of their employees, nor any of their contractors, subcontractors, or their employees, makes any warranty, express or implied, or assumes any legal liability or responsibility for the accuracy, completeness, or any third party's use or the results of such use of any information, apparatus, product, or process disclosed, or represents that its use would not infringe privately owned rights. Reference herein to any specific commercial product, process, or service by trade name, trademark, manufacturer, or otherwise, does not necessarily constitute or imply its endorsement, recommendation, or favoring by the United States Government or any agency thereof or its contractors or subcontractors. The views and opinions of authors expressed herein do not necessarily state or reflect those of the United States Government or any agency thereof.

In Situ Study of ABC Triblock Terpolymer Self-Assembly under Solvent Vapor Annealing

Sangho Lee[1], Li-Chen Cheng[1], Kevin G. Yager[2], Muhammad Mumtaz[3], Karim Aissou[3], and Caroline A. Ross*[1]

[1]Department of Materials Science and Engineering, Massachusetts Institute of Technology, Cambridge MA 02139, USA

[2]Center for Functional Nanomaterials, Brookhaven National Laboratory, Upton NY 11973, USA

[3]Laboratoire de Chimie des Polymères Organiques (LCPO), CNRS – ENSCPB – Université de Bordeaux, Pessac Cedex, France

for Table of Contents use only

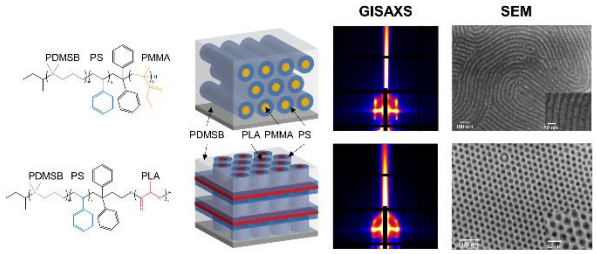

ABSTRACT: We investigate the morphological evolution of two linear ABC triblock terpolymers, poly(1,1-dimethyl silacyclobutane-*block*-styrene-*block*-methyl methacrylate) (PDMSB-*b*-PS-*b*-PMMA or DSM) and poly(1,1-dimethyl silacyclobutane-*block*-styrene-*block*-lactide) (PDMSB-*b*-PS-*b*-PLA or DSL) *in situ* during solvent vapor annealing using grazing-incidence small-angle X-ray scattering. The morphology, orientation, and period of the microdomains are characterized under a continuous solvent vapor flow of $CHCl_3$ as a function of swelling ratio and deswelling rate. 90 nm thick films of DSM form in-plane core-shell cylinders, while DSL films of 150 nm thickness predominantly form out-of-plane core-shell cylinders within perforated lamellae oriented parallel to the substrate. A reversible order-order phase transformation between spheres and cylinders and a reorientation from in-plane to out-of-plane cylinders occur during the annealing process.

KEYWORDS: self-assembly, grazing-incidence small-angle X-ray scattering, solvent vapor annealing, ABC triblock terpolymers, thin films.

INTRODUCTION

Self-assembled block copolymer (BCP) thin films have applications as membranes for separations,[1-3] in batteries,[4-5] as hydrophobic surfaces,[6] as active layers in photovoltaic devices,[7-8] and as templates for nanolithography.[9-12] In all these applications it is essential to control the morphology and orientation of the microdomains formed by microphase separation. Solvent vapor annealing (SVA) is particularly effective for tuning the BCP morphology *via* the solvent vapor pressure and composition,[13-17] swelling time and rate,[18] and drying rate.[14, 16, 19-20] In SVA the swelling ratio (SR) of the BCP film is highly dependent on the solvent composition and vapor pressure. The SR plays a crucial role in the structural organization and resultant morphology of the BCP.[13-18] For example, dilution of the solvent vapor with nitrogen gas can lead to reorientation and deformation of microdomains.[14, 16, 19-20] A continuous vapor flow system using bubblers allows independent adjustment of the vapor pressure of multiple solvent species, controlling each stage of the annealing process.[13, 16-17, 19-26]

In situ grazing-incidence small-angle X-ray scattering (GISAXS) has been employed to acquire real-time structural data from large areas of a sample at each stage of the self-assembly process,[15-17, 20, 25-30] providing averaged statistical information at specific times over a millimeter-size area, including morphology, period, orientation, and the long-range order of the microdomains.[31] Furthermore, this approach allows for observation of intermediate phases and order-order transitions during the annealing process.[15, 17, 28-29] The self-assembly process of diblock copolymers has been extensively explored by real-time GISAXS studies,[15-16, 20, 25, 27, 30] but there is limited work on the self-assembly of cyclic, branched or multiblock polymer architectures, such as cyclic block copolymers,[32] linear triblock terpolymers,[24, 28, 33-38] miktoarm star terpolymers,[21, 23, 39] and bottlebrush copolymers.[26, 32, 40-41] The phase behavior of multiblock

polymers is more difficult to elucidate using *ex situ* characterization due to their additional degrees of freedom and a wider range of morphologies. These morphologies can offer additional functionality, for example nanoscale ring structures formed from core-shell cylinders can exhibit desirable optical, electronic, and magnetic properties.[38, 42-44]

In this work, *in situ* GISAXS was used to study the self-assembly behavior of two linear ABC triblock terpolymers (TBTPs) during SVA in $CHCl_3$: poly(1,1-dimethyl silacyclobutane-*block*-styrene-*block*-methyl methacrylate) (PDMSB-*b*-PS-*b*-PMMA or DSM) and poly(1,1-dimethyl silacyclobutane-*block*-styrene-*block*-lactide) (PDMSB-*b*-PS-*b*-PLA or DSL). Thin films of DSM have been described previously, and exhibited a core-shell morphology on annealing in $CHCl_3$.[24] The DSL differs from DSM in replacing the PMMA end block with PLA which provides a hydrolysible block that can be selectively degraded for generating nanoporous thin films. In this work a continuous vapor flow system[13] was employed to control the vapor pressure of $CHCl_3$ during SVA. The structural evolution and the corresponding SR were measured by GISAXS in combination with spectral reflectometry, and compared with *ex situ* characterization of the final morphology based on scanning electron microscopy (SEM) observations.

RESULTS AND DISCUSSION

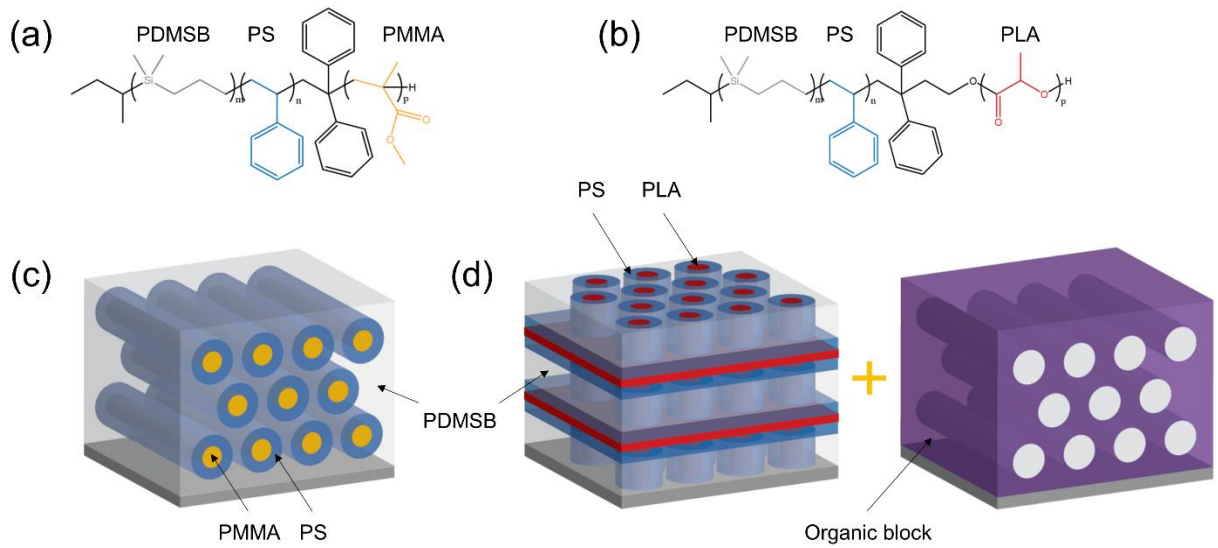

Figure 1. (a−b) Chemical structures and (c−d) schematic illustrations of DSM and DSL thin films. The proposed morphologies obtained in this study for each TBTP are presented: (c) hexagonally packed in-plane core-shell cylinders for DSM and (d) a coexistence of out-of-plane core-shell cylinders (left) and in-plane cylinders (right) for DSL. Schematics in white, blue, yellow, and red represent PDMSB, PS, PMMA, and PLA, respectively. The purple regions in the in-plane DSL morphology represent the organic blocks where the locations of the PS and PLA were not identified.

Both the DSM and DSL are linear triblock terpolymers synthesized *via* sequential anionic polymerization and are illustrated in Figure 1. The DSM has volume fractions f_{PDMSB} = 0.32, f_{PS} = 0.36, and f_{PMMA} = 0.32, a number average molecular weight (M_n) of 34 kg/mol, and a polydispersity index (PDI) of 1.10. The DSL has f_{PDMSB} = 0.31, f_{PS} = 0.53, and f_{PLA} = 0.16 with M_n = 38 kg/mol and PDI = 1.07. The morphologies of thick films of drop-cast DSM and DSL

after annealing in a solvent vapor flow of $CHCl_3$ were hexagonal (HEX), with center-to-center distances of ~ 41 nm and ~ 35 nm respectively (Figure S1). This spacing agrees with the results from the first-order peaks from synchrotron small angle X-ray scattering measurements of bulk samples, though in the bulk samples higher order peaks were not well resolved.

Films of the TBTPs with thickness 90 and 150 nm thick films were spin-coated on bare Si substrates with native oxide. This thickness is much larger than the period and can therefore yield films with multiple layers of in-plane oriented microdomains.[14, 16-18, 25, 30] Films were examined *in situ* by GISAXS during solvent annealing in $CHCl_3$. $CHCl_3$ was selected because it allows all the constituent blocks in DSM and DSL to swell enough for microphase separation to occur, and because it was used previously in solvent annealing of DSM[24] and other TBTPs.[21] After annealing and etching in an oxygen plasma, the final morphologies were characterized by SEM (see Experimental Section).

Both the GISAXS and O_2 plasma etching techniques are mainly sensitive to contrast between the PDMSB and the organic blocks due to the Si in the PDMSB. The Si causes the PDMSB block to have higher X-ray scattering and a higher resistance to oxygen etching compared to the PS, PMMA, and PLA. Thus, the scattering contrast in the GISAXS images originates primarily from the arrangement of the PDMSB microdomains, and is insensitive to the microphase separation of PS and PLA or PS and PMMA. Oxygen etching removes the organic blocks in DSM and DSL leaving silica-rich oxidized PDMSB features, though the PDMSB is less etch resistant than polydimethylsiloxane, a commonly used Si-containing block[45-47]. Additional etching processes were employed including the UV degradation of PMMA[30] and the hydrolysis of PLA[48,] which enable the PMMA or PLA blocks to be distinguished from the PS.

A thin PDMSB layer is observed at the air/TBTP and TBTP/substrate interfaces[23-24] indicating that PDMSB has a lower surface energy compared to PS, PMMA and PLA, whose surface energies are ~ 40 mJ/m^2.[38] PDMSB surface layers were selectively removed by a CF_4 etching step.

Figure 1 illustrates schematically the structures which we propose for the TBTP films, based on the SEM and GISAXS data presented in this article. We found that both DSL and DSM formed core-shell cylinder structures in the solvent-annealed thin films, but the orientation and the detailed morphology of the microdomains differed between the two polymers and were affected by the annealing conditions.

Phase Behavior of PDMSB-*b*-PS-*b*-PMMA (DSM)

We first describe the evolution of the HEX morphology in DSM films during SVA in $CHCl_3$. Figure 2a shows the swelling ratio *vs.* time for the SVA processes, and Figures 3 and S2 show the GISAXS images. The maximum SR and the deswelling rate of the film were adjusted by changing the amount of nitrogen added to the solvent flow. For a film with an as-cast thickness of 90 nm, SR = 2.3 was obtained using a vapor flow of $CHCl_3$:N_2 = 10:1, *i.e.* 10 sccm of $CHCl_3$ vapor plus 1 sccm of N_2 flow (process A and B), while SR = 2.0 was obtained using $CHCl_3$:N_2 = 8:2 (process C), as shown in Figure 2a. The solvent was rapidly removed from the chamber by 100 sccm of N_2 flow in process A, whereas the film was more slowly deswelled using 3 sccm of N_2 for ~ 10 min and subsequently quenched with 100 sccm of N_2 flow in process B and C.

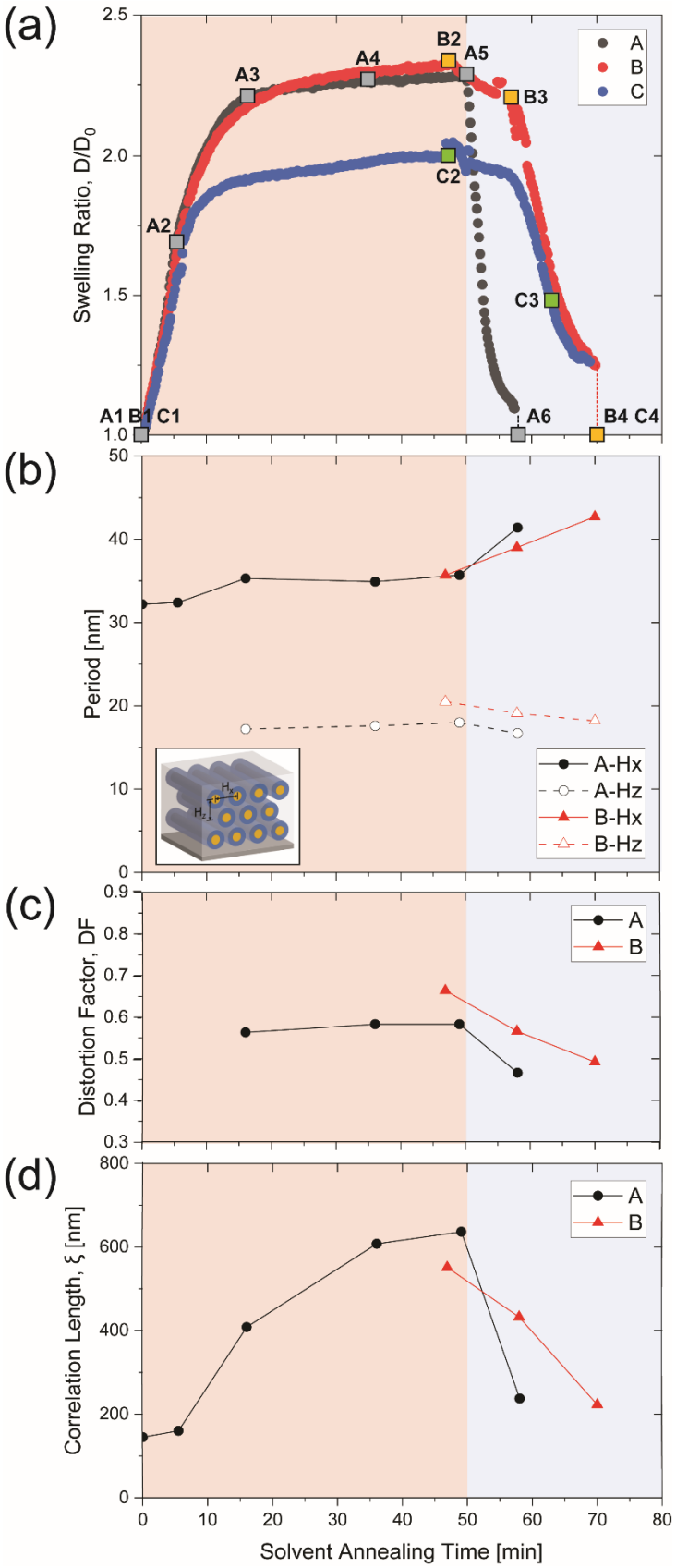
(a)
Swelling Ratio, D/D0
A
B
C
A1 B1 C1
A2
A3
A4
B2
A5
B3
C2
C3
A6
B4 C4
(b)
Period [nm]
A-Hx
A-Hz
B-Hx
B-Hz
(c)
Distortion Factor, DF
A
B
(d)
Correlation Length, ξ [nm]
A
B
Solvent Annealing Time [min]

Figure 2. Quantitative analysis of evolution of (a) swelling ratio, (b) period, (c) distortion factor, and (d) correlation length as a function of solvent annealing time for DSM films with as-spun thickness of 90 nm. Swelling ratios were determined in a solvent vapor flow of $CHCl_3/N_2$ = 10:1 (processes A and B) and $CHCl_3/N_2$ = 8:2 (process C). The film in process A was quenched and films in processes B and C were slowly deswelled. Processes A, B, and C are represented by black, red, and blue circles, respectively. H_x and H_z in (b) indicate in-plane period and out-of-plane spacing between layers of cylinders respectively as described in the inset.

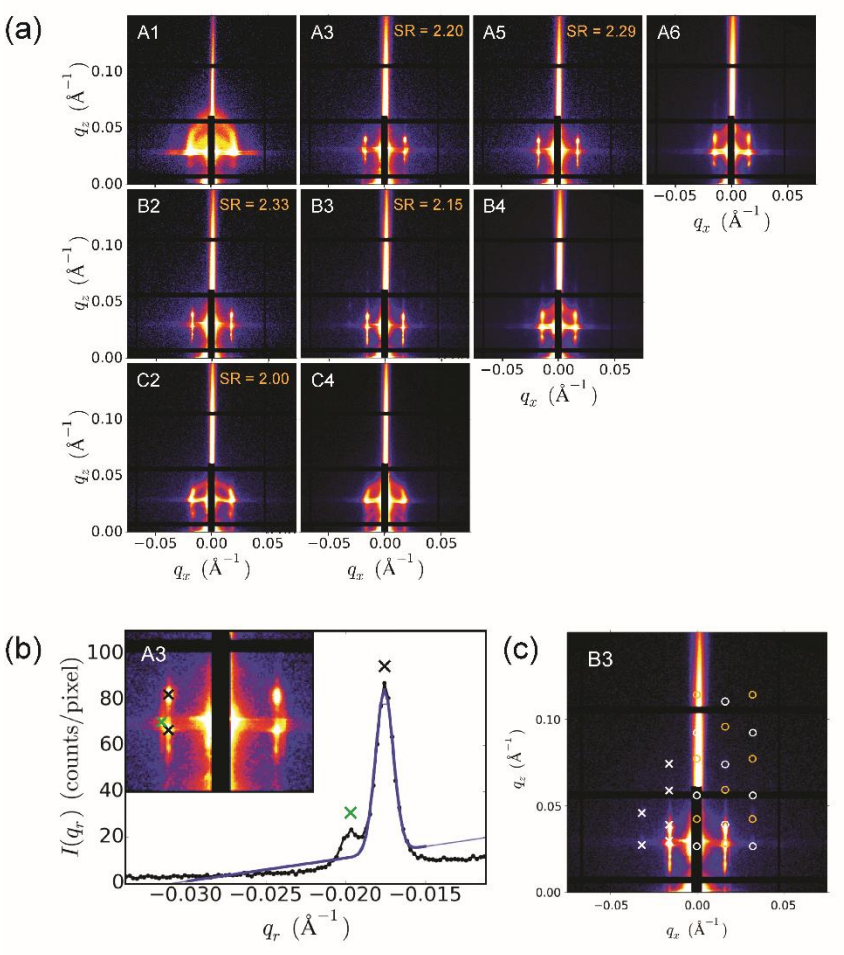

Figure 3. (a) GISAXS patterns showing the morphological evolution of DSM films in processes A, B, and C. The scattering profile corresponds to the stage marked on the swelling ratio (SR) curve in Figure 2a. SR at each stage is noted on the upper right corner of the panel. (b) In-plane linecut of scattering intensity $I(q_r)$ *vs.* q_r in Å^{-1} for A3, with inset showing the magnified GISAXS 2D image. The scattering peaks in both the intensity curve and the image indicating in-plane and out-of-plane oriented cylinders are marked by black and green crosses, respectively. The linecut graph is fitted by the blue curve from which H_x = 35.8 nm at point A3 is determined, as described in Figure 2b. (c) GISAXS pattern at point B3 with actual peaks (crosses) and expected spots for a HEX lattice (circles). The yellow and white circles correspond to the direct and reflected beams, respectively.

The scattering pattern of the as-cast film (point A1 in Figure 3) initially displayed a broad isotropic (and somewhat elliptic) ring, consistent with a disordered morphology of randomly-oriented micellar-like domains, and typical of the kinetically trapped as-cast state of BCPs.[15-17, 25, 28, 30] GISAXS patterns started to show clear peaks indicating a HEX structure early in the SVA processing. This is attributed to hexagonally close-packed (HCP) cylindrical microdomains with a coexistence of in-plane and out-of-plane orientations, which formed as the film was rapidly swelled up to SR = 2.20 (A3). Based on the relative intensity of scattering peaks analyzed from each set of GISAXS data as exemplified in Figure 3b, the fraction of out-of-plane oriented cylinders was about a quarter that of the in-plane cylinders at point A3. The out-of-plane cylinders gradually transformed to in-plane cylinders as annealing proceeded for ~ 50 min (A5), and the film maintained its in-plane cylinder orientation after the quenching process (A6) even though the BCP period and the correlation length ξ changed. The correlation length or 'grain size' of the in-plane cylinders is calculated from the scattering peak width (see Experimental Section). Scattering peaks became broader during the solvent desorption, which represents a decrease in order, presumably due to the rearrangement of the polymer to accommodate the volume shrinkage from solvent loss during deswelling.

We believe that the HEX structure indicated by the GISAXS data consists of cylinders of a PMMA core with a PS shell within a PDMSB matrix as depicted in Figure 1c. Selective removal of PMMA microdomains following UV irradiation confirmed that the PMMA was present at the centers of the cylinders, Figure S3. This is consistent with previous experimental results of the identical TBTP annealed in $CHCl_3$ which exhibited core-shell cylinders.[24] The formation of a core-shell structure is attributed to a change in the volume fraction during exposure to the $CHCl_3$ vapor, due to the different affinity of each block to the solvent indicated by the difference in

solubility parameters. The PDMSB block has the highest affinity for $CHCl_3$ and swells more than PS and PMMA leading to a higher effective volume fraction of PDMSB, so it forms the matrix of the core-shell cylinders. For the same TBTP, a transition from out-of-plane oriented cylinders to in-plane oriented cylinders occurred for film thickness of 47 nm and above,[24] which is consistent with the in-plane orientation observed here in the deswelled films. A simulation for a TBTP in which the interaction parameter between the end blocks is the largest predicts a morphology consisting of core-shell cylinders or alternating lamellae.[34] The room temperature interaction parameters are $\chi_{PS\text{-}PMMA} \approx 0.04$,[49] $\chi_{PDMSB\text{-}PS} \approx 0.07$,[23] and $\chi_{PDMSB\text{-}PMMA} \approx 0.2$,[24] and core-shell morphology is stabilized because it avoids interfaces between the two blocks (PDMSB and PMMA) with the largest χ-parameter.

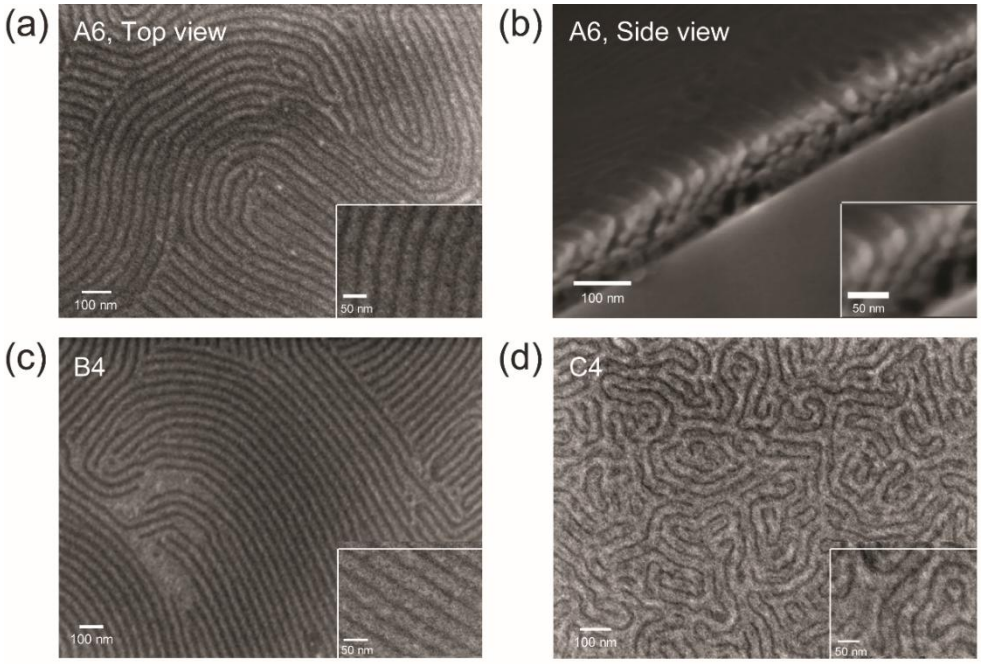

Figure 4. SEM images of the final morphologies in DSM thin films for processes A, B, and C. All the images show oxidized PDMSB nanopatterns for (a−b) A6, (c) B4, and (d) C4. All the scale bars in the main images are 100 nm and in the insets are 50 nm.

Process B demonstrates the effect of a slower solvent desorption rate. Overall, the film behaved similarly to that of process A, producing in-plane cylinders as shown in the SEM images (Figure 4) as well as from the GISAXS patterns (Figure 3). However, process B gave rise to more intense high-order scattering peaks during deswelling, shown in B3, indicative of a morphology with better long-range positional order.

Figure 2b−d shows a quantitative analysis of the structural evolution of DSM in processes A and B in terms of the in-plane period H_x, out-of-plane spacing between layers of cylinders H_z, distortion factor (DF), and correlation length ξ. DF is defined as $2H_z/\sqrt{3}H_x$ which is 1 for an ideal HCP array with nearest-neighbor layers parallel to the substrate. The two samples had small differences in the SR as a function of time during the initial 50 min of the solvent annealing, even though the swelling conditions were nominally the same. H_z = 18 nm for process A and H_z = 21 nm for process B immediately before deswelling.

As described in Figure 2b, H_x and H_z increased by only ~ 3 and ~ 1 nm respectively as the films swelled. However, during the drying process H_x increased further by 6 – 7 nm while H_z decreased by only 1 – 2 nm. These changes lead to a decrease in distortion factor. Based on H_z and the total film thickness, we deduce that the number of layers of cylinders in the film changed from about 10 to 5 during the deswelling. This differs from observations in PS-*b*-PDMS, where H_z decreased as the film deswelled.[16] This suggests that there is a significant rearrangement of polymer chains during the solvent desorption to maintain the value of H_z. Process B also showed a decrease in DF during the deswelling, though the changes occurred more gradually.

The correlation length ξ, Figure 2d, increased for annealing times up to 50 min as the ordering of the microdomains improved. It decreased as the films deswelled, reaching the same final value of ~ 200 nm in the dry state for both processes A and B.

SEM images of the final morphology, Figure 4, show good agreement with GISAXS results in terms of the structure and the period. From SEM in Figure 4 and S3, H_x = ~ 42 nm and H_z = ~ 18 nm for both processes A and B, which are similar to the values obtained from GISAXS. As mentioned earlier, the X-ray scattering is most sensitive to contrast between the PDMSB block and the organic blocks, and the data do not resolve the core-shell arrangement of the PS and PMMA blocks. Thus, the GISAXS peaks in Figure 3 originate from the periodicity of the PS/PMMA cylinders within the PDMSB matrix.

During etching, the O_2 plasma not only removes the organic core-shell cylinders but also reduces the volume of the exposed PDMSB microdomains as they are converted to a silica-rich composition. In the top view image, thin ridges from the PDMSB matrix are visible (Figure 4 and S4) and in the cross-section image (etched only in oxygen) the junction points of the PDMSB matrix, which occur between each set of three core-shell cylinders, protrude to form the arrangement shown schematically in Figure S4.

In process C, the maximum SR was reduced to 2.0 *vs.* 2.25 for processes A and B. The GISAXS data (Figure 3) indicated cylinders in various orientations with respect to the substrate and a ξ of 160 nm at the end of annealing, and SEM (Figure 4d) shows short, poorly ordered cylinders. The lower SR leads to less chain mobility and slower diffusion, but the center-to-center spacing of the final structure was 41 nm, almost the same as that for process A and B. Thus, the in-plane periodicity of microdomains evolves to a value regardless of SR that is close to the value of 38 nm reported for out-of-plane oriented cylinders of the same TBTP.[24]

Phase Behavior of PDMSB-*b*-PS-*b*-PLA (DSL)

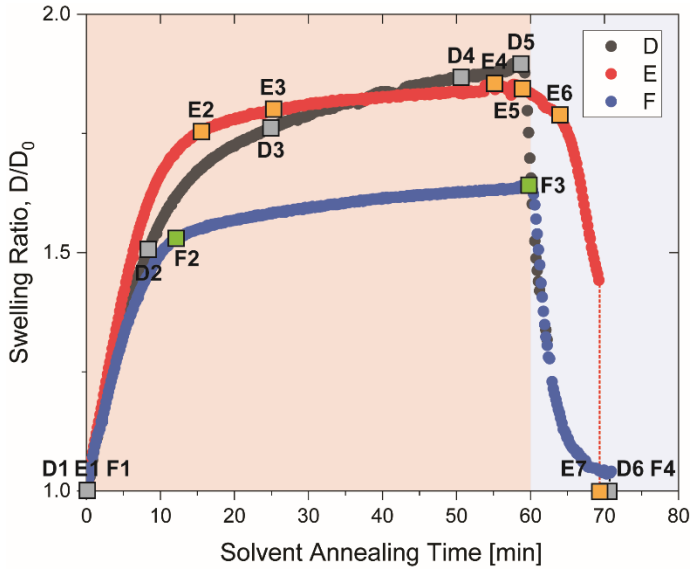

Figure 5. Swelling ratios of DSL films with as-cast thickness of 150 nm in a solvent vapor flow of $CHCl_3/N_2$ = 10:1 (processes D and E) and $CHCl_3/N_2$ = 8:2 (process F), respectively. Films in processes D and F were quickly deswelled and the film in process E was slowly deswelled. Processes D, E, and F are represented by black, red, and blue circles, respectively.

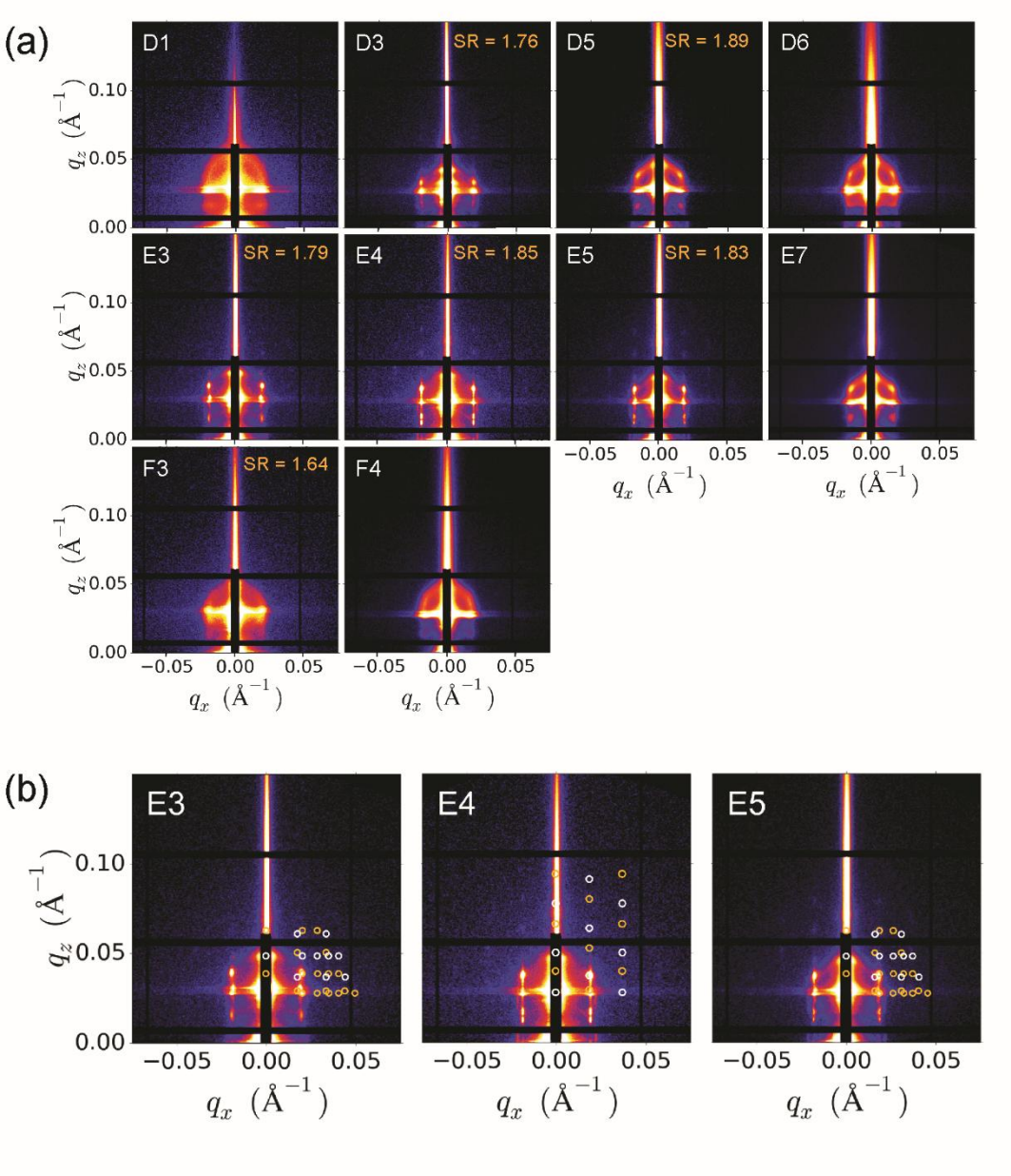

Figure 6. (a) GISAXS patterns showing the morphological evolution of DSL films in processes D, E, and F. The scattering profile corresponds to the stage marked on the swelling ratio curve in Figure 5. SR at each stage is noted on the upper right corner of the panel. (b) Scattering patterns at stages E3, E4, and E5 are shown overlaid with the expected spots for BCC (110), HEX, and BCC (110) lattices, respectively. Yellow and white circles correspond to the direct and reflected beams.

We now discuss the structural transitions of 150 nm thick DSL films during SVA in $CHCl_3$ using *in situ* GISAXS. Figure 5 shows the SR during the annealing processes D, E and F, which were nominally the same sequence of gas flow as processes A, B and C respectively. Figure 6 and S5 show the GISAXS data. A SR of ~ 1.9 (process D and E) was achieved under a vapor flow of $CHCl_3/N_2$ = 10:1, while SR ~ 1.6 under $CHCl_3/N_2$ = 8:2 (process F). The rate of deswelling was changed by using a N_2 flow of 100 sccm (process D and F, fast deswelling) and N_2 flow of 3 sccm for ~ 10 min followed by 100 sccm (process E, slow deswelling).

As the solvent swelled the film in process D, a HEX structure attributed to close-packed in-plane cylinders (Figure 6, D3) was formed starting from the disordered structure (D1). Beyond this stage, both in-plane and out-of-plane HEX microdomains coexisted at the maximum SR of 1.89 (D5). When the swollen film was quenched by the N_2 flow, it maintained the same overall morphology, but the proportion of out-of-plane cylindrical microdomains increased during the solvent desorption, based on the intensity of scattering peaks. The GISAXS data of the dried film (D6) showed peaks from both an out-of-plane HEX structure with nearest neighbor spacing H_p of 35 nm and from in-plane distorted HEX with H_x of 42 nm and H_z of 18 nm.

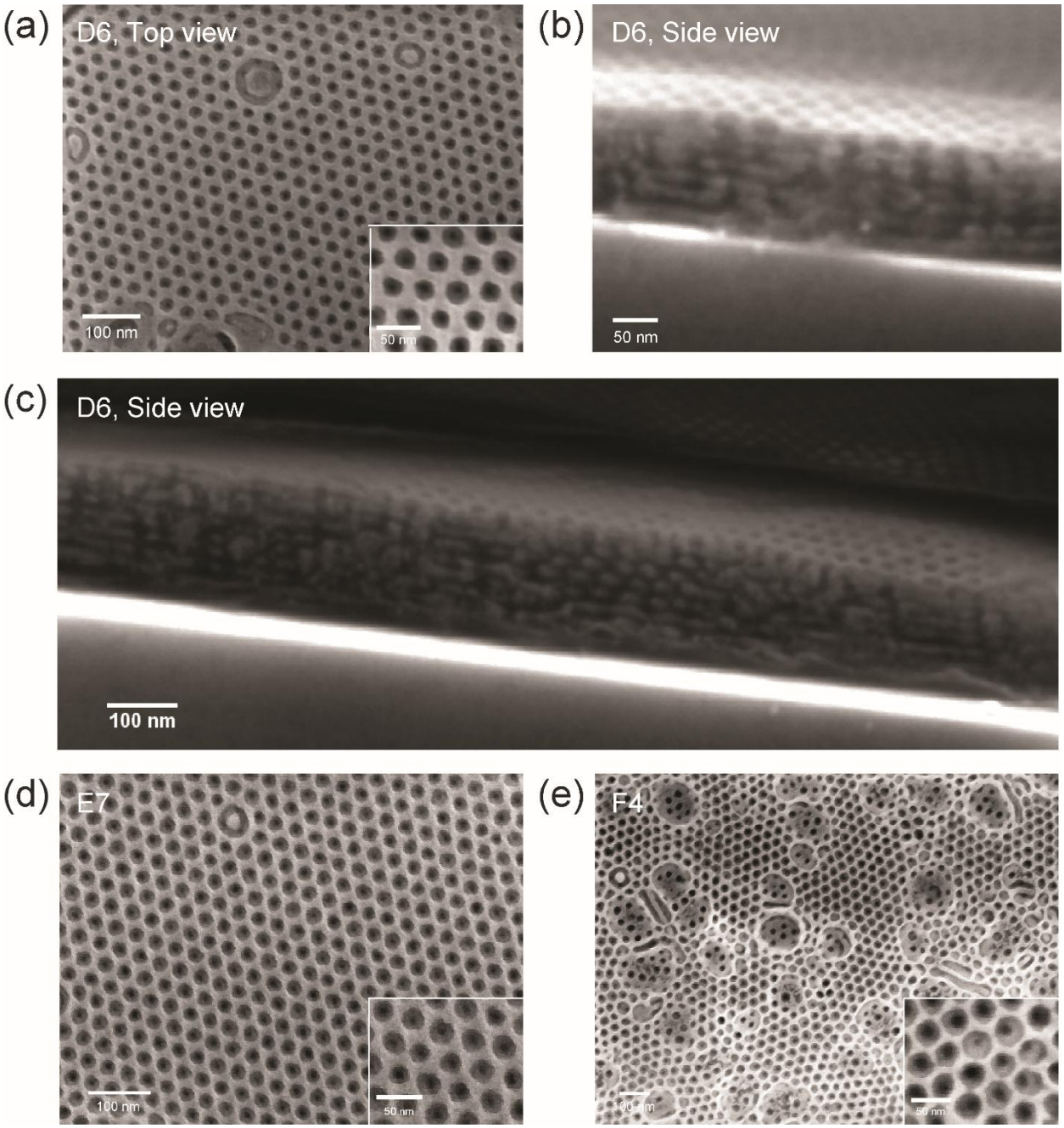

Figure 7. SEM images of the final morphologies in DSL thin films for processes D, E, and F. All the images mainly show oxidized PDMSB nanopatterns for (a−c) D6, (d) E7, and (e) F4; PS and PLA blocks forming core-shell cylinders are also distinguished due to their difference in etch resistance. Scale bars in the main images of (a, c-e) and (b) are 100 and 50 nm. All the scale bars in the insets are 50 nm.

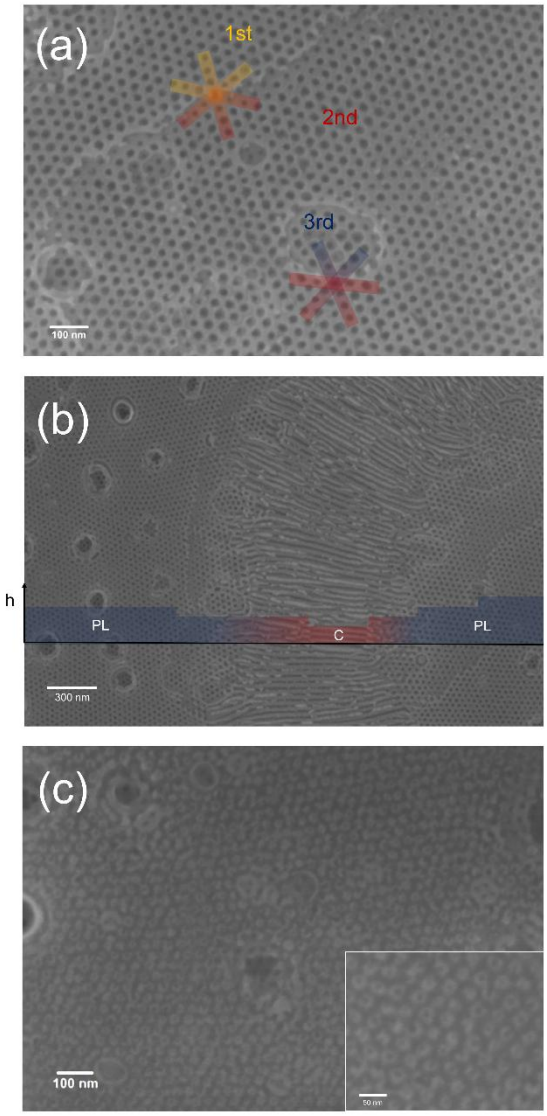

Figure 8. SEM images of the final morphologies in DSL thin films: plan view of terraces formed due to the additional CF_4/O_2 etching process showing (a) multiple layers of PL and (b) a coexistence of multilayer PL and C. Holes in the top (yellow), second (red), and third (blue) layers in (a) are aligned above each other as emphasized by the colored lines drawn to show that the lattice of pores is continuous across two adjacent layers. The height profile across the black line is depicted in (b) and the morphology of each layer is either PL (blue) or C (red). (c) A hexagonal array of PS nanorings resolved by a CF_4/O_2 plasma etching process.

SEM images of the final morphology in Figure 7 show both in-plane and out-of-plane periodicity. The top surface shows a close-packed arrangement corresponding to perpendicular cylinders or a perforated lamella (PL), and the insets of Figure 7 show a core-shell structure within the pores which originates from the different etching behavior of the PLA and PS blocks in the O_2 plasma. By using CF_4 and O_2 plasma to selectively degrade the PDMSB and PLA microdomains, respectively, a vertically aligned PS nanoring array was observed corresponding to the shells of the cylinders (Figure 8c). The nearest neighbor spacing of 35 nm matched the GISAXS result.

The cross-sectional images in Figure 7 and S6 show two different layered structures in different regions of the cross-section. The dominant morphology (e.g. Figure 7b) was an in-plane layered structure with spacing ~ 21 nm (similar to H_z from GISAXS) and with vertical features that go through the film thickness, corresponding to the core-shell cylinders seen at the top surface. To examine this morphology in more detail, we etched only a part of the top surface in CF_4/O_2 plasma (see Experimental Section) to resolve the structure of the interior layers in plain view (Figure 8 and S6). As shown in Figure 8a, this process revealed terraces of PL PDMSB in which the pores were vertically aligned through the separate layers of PL, i.e. the stacked pores define the locations of the PLA/PS core-shell cylinders which are oriented perpendicular to the film.

The PDMSB forms in-plane perforated lamellae because it has insufficient volume fraction to form a continuous matrix surrounding the cylinders. We believe that the PDMSB PL are separated by majority PS layers sandwiching a thin PLA layer, shown schematically in the left panel of Figure 1d. The presence of in-plane PLA layers was revealed by selectively degrading

the PLA through hydrolysis as described in Figure S8. This arrangement may be favored by the preferential wetting of the air and substrate by PDMSB.

In other regions of the cross-section (e.g. right of center in Figure 7c), the structure shows in-plane cylinders of PDMSB with H_x = ~ 40 nm and H_z = ~ 21 nm. The in-plane cylinders are also seen in the top view after etching, Figure 8b. This is consistent with a morphology of alternating PDMSB and PLA cylinders in a PS matrix, although the PLA cannot be clearly resolved even by the hydrolysis of PLA due to its low volume fraction. The structure is illustrated in the right panel of Figure 1d where the purple shading represents the location of the combined PLA and PMMA blocks.

GISAXS results for process E provide further information on the morphological evolution of the DSL film during the annealing process (Figure 6). As shown in Figure 5, for process E the SR increased more rapidly than in process D and reached a lower maximum value although the processes were nominally the same before deswelling started. Interestingly, the film exhibited a spherical morphology at stage E3 during the swelling and E5 during the deswelling, and an in-plane HEX structure formed at the maximum SR of 1.85 (E4) with H_x = 35 nm and H_z = 19 nm. Based on the modeled GISAXS peaks for the (110) plane of a body-centered cubic (BCC) lattice in Figure 6 and S7, the spherical morphologies at point E3 and E5 correspond to 23 % and 34 % compressed BCC structures with nearest-neighbor distance of 35 nm, given that the scattering peaks were stretched along the z-direction in reciprocal space.[15] Similar to process D, the dry film exhibited a morphology with coexisting in-plane and out-of-plane periodicity. However, the GISAXS pattern at stage E7 in Figure 6 showed that a larger fraction of the microdomains was aligned in-plane after the slower drying compared to process D (D6). The *in situ* GISAXS

therefore demonstrates that the DSL morphology is sensitive to SR, and that a reversible order-order phase transition between spheres and cylinders can occur on changing the SR.

For process F, which had a maximum SR of 1.64, the swelled film did not form either spheres or in-plane HEX (Figure S5) and it eventually produced an out-of-plane HEX morphology with H_x = 35 nm at the end of deswelling (Figure 6). The final structure according to SEM (Figure 7e) is consistent with GISAXS results and exhibits core-shell cylinders oriented out-of-plane. However, the defectivity was higher and the order was poorer compared to process D and E. The degradation in order at lower SR is consistent with the results of the DSM polymer in process C.

To interpret the structure of the DSL films, we consider predictions based on the asymmetric volume fraction (D:S:L = 31:53:16). Self-consistent field theory (SCFT) modeling predicts that the bulk morphology of a nonfrustrated linear TBTP such as DSL ($\chi_{DL} > \chi_{LS} > \chi_{DS}$)[23] at this volume composition can consist of a core-shell hexagonal lattice of cylinders or two interpenetrating tetragonal lattices.[34] In the former case the large volume fraction of the middle block would be accomodated in the relatively thick shell of the core-shell cylinders, and the core consists of the smallest volume fraction block (here, PLA). These calculations were limited to two dimensions so cannot account for variations in the third dimension such as spherical morphologies. The thin film geometry provides further constraints due to surface energy and commensurability effects.

As discussed above, the DSL film includes regions with two different morphologies. The majority of the cross-sectional image is consistent with a morphology consisting of vertical core-shell cylinders, surrounded by a matrix consisting of perforated lamellae of PDMSB separated by PS and PLA layers. In other examples of thin film multilayer PL morphologies, such as in a PS-

b-PDMS-b-PS triblock copolymer,[17] the pores in one PL layer overlay junctions in the adjacent layer. The DSL instead shows alignment of the pores in the layers above each other, and we speculate that this could indicate that the out-of-plane cylinders formed before the PL, defining the pore locations.

For the in-plane cylinder morphology, the PDMSB cylinders visible in the SEM cross-section are hexagonally packed instead of forming the tetragonal lattice expected from simulation results.[34] Other TBTPs show a transition between HEX core-shell cylinders and tetragonal alternating cylinders depending on film thickness[36] including regimes where both morphologies were present.

We summarize the experimental conditions and final morphologies and periods of the DSM and DSL thin films in Table 1. The intermediate phases are also listed to convey the structural transitions during the annealing process. Overall, the final structures had little dependence on the major annealing variables of the study: deswelling rate and SR. However, the proportion of out-of-plane *vs.* in-plane cylinders in DSL films changed with the solvent desorption rate, and a low SR prevented both TBTPs from forming well ordered structures. DSL in particular shows only out-of-plane cylinders for low SR, while it exhibits a morphology with a coexistence of vertically aligned cylinders and in-plane cylinders for high SR. Furthermore, the same morphology produced under different annealing conditions had almost the same center-to-center spacing. As expected, the periodicity of the DSL film was also maintained during the order-order transition.

Table 1. Summary of solvent vapor annealing conditions and resultant morphologies and periods of DSM and DSL thin films.

	Process	As-cast thickness [nm]	Swell time [min]	Swell condition ($CHCl_3/N_2$) [sccm]	Deswell condition (N_2) [sccm]	Morphology	Nearest-neighbor distance [nm][a)]
DSM							
A	A6			10:1	100	$Hex_{//}$	41
B	B4	90	50	10:1	3 (10 min) + 100	$Hex_{//}$	43
C	C4			8:2	3 (10 min) + 100	Poorly ordered Hex	41
DSL							
D	D6			10:1	100	$Hex_{\perp}$ ($Alt_{//}$)	35 (42)
E	E3					BCC (110)	35
	E4	150	60	10:1	3 (10 min) + 100	$Hex_{//}$	35
	E5					BCC (110)	35
	E7					$Hex_{\perp}$ ($Alt_{//}$)	35 (42)
F	F4			8:2	100	Poorly ordered $Hex_{\perp}$	35

Hex, hexagonally packed core-shell cylinders; Alt, hexagonally packed alternating cylinders; BCC, body-centered cubic spheres; //, parallel alignment; $\perp$, out of plane alignment; [a)]Estimated from GISAXS results.

CONCLUSION

The microphase separation of film of two TBTPs (DSM and DSL) was tracked using *in situ* GISAXS to understand the structural organization of the different blocks during solvent annealing in a continuous vapor flow system. GISAXS provides rich details of dynamic transformations from the disordered to the ordered state during annealing that are not observed using *ex situ* characterization techniques. DSM films formed core-shell PMMA-PS cylinders oriented in-plane with a distorted hexagonal packing within a PDMSB matrix. The core-shell structure is a result of the selectivity of the solvent to PDMSB and the highest interaction parameter being that between the end blocks, $\chi_{PDMSB\text{-}PMMA}$. DSL films showed a reversible order-order transition between spheres and cylinders during self-assembly. The final morphology of the DSL consisted partly of regions of in-plane cylinders, but mainly of regions of out-of-plane core-shell PLA-PS cylinders passing through perforated lamellae of PDMSB such that the pores of the PL are stacked vertically. The DSL also exhibited such a structure, which exhibits both vertical and lateral features, may be useful in fabricating three-dimensional devices.

EXPERIMENTAL SECTION

Materials and Preparation of TBTP Films. Linear PDMSB-*b*-PS-*b*-PMMA (DSM) and PDMSB-*b*-PS-*b*-PLA (DSL) triblock terpolymers were synthesized *via* sequential anionic polymerization. More details concerning the synthesis of these polymers can be found in Ref (24). Thick film morphologies of DSM and DSL (Figure S1) were obtained from drop-cast films deposited from a mixture of tetrahydrofuran and propylene glycol monomethyl ether acetate (THF/PGMEA = 2:1) onto oxidized silicon substrates and annealed in a solvent vapor flow of $CHCl_3$ (10 sccm) for 1 h. Thin DSM and DSL thin films were spin-coated on silicon substrates with native oxide layer from 3 – 4 wt% solutions in a mixture of THF and PGMEA. As-cast film thickness of DSM (t = 90 nm) and DSL (t = 150 nm) were determined by adjusting the spin speeds (3,000 – 10,000 rpm) and measured values were obtained from a spectral reflectometer (FilMetrics F20-UV). All the solvents used in this study were purchased from Sigma Aldrich.

Solvent Vapor Annealing and *In situ* GISAXS Measurement. SVA and GISAXS experiments were performed at the Complex Materials Scattering (CMS, 11-BM) beamline of the National Synchrotron Light Source II at Brookhaven National Laboratory. As-cast DSM and DSL films on substrates were placed inside a custom solvent annealing cell, and the cell was mounted inside the measurement chamber.[16] The small cell was airtight and it included two Kapton windows for the incident X-ray the scattered X-ray beams. The lid of the cell included a quartz window to allow real-time monitoring of film thickness *via* UV−vis spectral reflectometry (FilMetrics). An inflow tube and solvent exhaust tube were present to enable control of the atmosphere within the chamber. SVA was carried out using a continuous flow system where separate streams of nitrogen are bubbled through liquid solvents and the flow of each stream is regulated using a

mass flow controller (MKS Inc., M100B).[13] The inflow tube was connected to a mixer fed by two flow channels: pure N_2 gas (Airgas, Inc., 99.9997% purity) for controlling the solvent absorption and desorption rate and a solvent bubbler which contained $CHCl_3$. DSM and DSL samples were annealed in a vapor flow of $CHCl_3$ and N_2 for 50 min and 1 h respectively. For both polymers, solvent vapors of $CHCl_3$:N_2 = 10:1 and 8:2 were introduced to achieve high SR and low SR respectively, where the numbers represent the flow rate in sccm for $CHCl_3/N_2$. During the deswelling, swollen films were rapidly or slowly dried by injecting pure N_2 flow of 100 sccm or 3 sccm for 10 min and 100 sccm subsequently.

The X-ray beam energy was set to 13.5 keV (X-ray wavelength 0.918 Å) using a multilayer monochromator. The beam size was set to 200 μm (horizontal) by 50 μm (vertical) to limit the projected area of X-ray illumination on the sample. Small-angle scattering data was collected on a photon-counting pixel-array area detector (Dectris Pilatus 2M) positioned 5.09 m downstream of the sample. Conversion of scattering images to reciprocal-space (q) was accomplished by measuring a silver behenate powder as a calibration standard. We define q_z to be the vertical direction (film normal direction) and q_x as the orthogonal horizontal (in-plane) direction. GISAXS images were taken at periodic increments of time to probe any changes occurring within the film during SVA. The film was moved slightly across the beam for each new exposure, in order to limit X-ray beam induced damage, which can give rise to modifications of the self-assembled morphology due to cross-linking and/or chain scission.[50] Analysis of GISAXS data was performed by taking linecuts through the q-calibrated data. Repeat spacing was measured by fitting the position of the first-order scattering peak, and converting to real space in the usual manner ($H = 2\pi/q$). For the vertical repeat spacing of the morphology (q_z peak position), we accounted for the distortion of reciprocal space due to refraction of the incident and scattered

rays, using a value for the film's average electron density consistent with the measured position of the Yoneda scattering. Material correlation length was calculated from the scattering peak width using a Scherrer-like formalism, while accounting for instrumental resolution effects.[51]

Characterization of TBTP Films. An additional sample was simultaneously annealed in the solvent annealing cell for each experiment in order to obtain a film showing the final state that was not affected by the X-ray beam. To enhance the imaging contrast, the PDMSB surface layer and microdomains of organic blocks (PS, PMMA, and PLA) in annealed DSM and DSL thin films were selectively removed by reactive ion etching (RIE, Plasma-Therm 790) treatment with CF_4 (5 s, 15 mTorr, 50 W) and O_2 (22 s, 6 mTorr, 90 W), respectively. For bulk (Figure S1) samples, we used a longer RIE with CF_4 (60 s, 15 mTorr, 50 W) to observe buried microdomains. Terraced regions of PDMSB in Figure 8 and S6 were obtained by covering the half of the sample, etching the exposed half with CF_4 (60 s, 15 mTorr, 50 W) and O_2 (22 s, 6 mTorr, 90 W), and imaging the boundary of these two regions. This process yields oxidized PDMSB patterns that exhibit the internal morphology of the PDMSB microdomains arising from the respective annealing conditions. It was possible to distinguish PS and PLA microdomains in the DSL films without an additional staining process because they have slightly different etch resistance to O_2 RIE plasma.

For the UV degradation of PMMA, a cross-section of DSM sample was exposed to UV radiation (5 mW/cm^2 and λ = 253.7 nm) for 1200 s and followed by RIE with O_2 (10 s, 6 mTorr, 90 W). For the hydrolysis of PLA, a 0.5 M solution was prepared by dissolving sodium hydroxide in a 40:60 v/v% solution of methanol and water and a DSL sample was placed in the aqueous methanol solution at 65 °C for 48 h. After the hydrolytic process, the sample was rinsed

with water and methanol and dried under vacuum at room temperature. After dry and wet etch processes, the etched TBTP films were imaged using a Zeiss Merlin high-resolution SEM at 3 kV. The cross-sections were prepared by cracking the sample in liquid nitrogen followed by RIE with O_2 (5 s, 6 mTorr, 90 W) and imaged after tilting the sample 70° to the SEM detector in order to show the morphology of both the top and cross-section surfaces.

ASSOCIATED CONTENT

Supporting Information

Supporting Information is available free of charge on the ACS Publications website at DOI: 10.1021/acs.macromol.

Additional information on bulk morphologies, GISAXS patterns at all the labeled stages of solvent annealing conditions, and selectively etched cross-sectional SEM images with schematic illustrations for DSM and DSL films

AUTHOR INFORMATION

Corresponding Author

*E-mail: caross@mit.edu (C.A.R.).

Notes

The authors declare no competing financial interest.

ACKNOWLEDGMENTS

This work was supported by NSF DMR-1606911. Shared experimental facilities of CMSE, an NSF MRSEC under award DMR-1419807, were used. This research used resources of the Center for Functional Nanomaterials, and the National Synchrotron Light Source II, which are U.S. DOE Office of Science Facilities, at Brookhaven National Laboratory under Contract No. DE-SC0012704.

REFERENCES

(1) Yang, S. Y.; Ryu, I.; Kim, H. Y.; Kim, J. K.; Jang, S. K.; Russell, T. P. Nanoporous Membranes with Ultrahigh Selectivity and Flux for the Filtration of Viruses. *Adv. Mater.* **2006**, *18*, 709−712.

(2) Jackson, E. A.; Hillmyer, M. A. Nanoporous Membranes Derived from Block Copolymers: From Drug Delivery to Water Filtration. *ACS Nano* **2010**, *4*, 3548−3553.

(3) Ahn, H.; Park, S.; Kim, S.-W.; Yoo, P. J.; Ryu, D. Y.; Russell, T. P. Nanoporous Block Copolymer Membranes for Ultrafiltration: A Simple Approach to Size Tunability. *ACS Nano* **2014**, *8*, 11745−11752.

(4) Orilall, M. C.; Wiesner, U. Block Copolymer Based Composition and Morphology Control in Nanostructured Hybrid Materials for Energy Conversion and Storage: Solar Cells, Batteries, and Fuel Cells. *Chem. Soc. Rev.* **2011**, *40*, 520−535.

(5) Sing, C. E.; Zwanikken, J. W.; Olvera de la Cruz, M. Electrostatic Control of Block Copolymer Morphology. *Nat. Mater.* **2014**, *13*, 694−698.

(6) Checco, A.; Rahman, A.; Black, C. T. Robust Superhydrophobicity in Large-Area Nanostructured Surfaces Defined by Block-Copolymer Self Assembly. *Adv. Mater.* **2014**, *26*, 886−891.

(7) Darling, S. B. Block Copolymers for Photovoltaics. *Energy Environ. Sci.* **2009**, *2*, 1266−1273.

(8) Guo, C.; Lin, Y. H.; Witman, M. D.; Smith, K. A.; Wang, C.; Hexemer, A.; Strzalka, J.; Gomez, E. D.; Verduzco, R. Conjugated Block Copolymer Photovoltaics with near 3% Efficiency through Microphase Separation. *Nano Lett.* **2013**, *13*, 2957−2963.

(9) Gu, X.; Liu, Z.; Gunkel, I.; Chourou, S. T.; Hong, S. W.; Olynick, D. L.; Russell, T. P. High Aspect Ratio Sub- 15 nm Silicon Trenches From Block Copolymer Templates. *Adv. Mater.* **2012**, *24*, 5688−5694.

(10) Ross, C. A.; Berggren, K. K.; Cheng, J. Y.; Jung, Y. S.; Chang, J.-B. Three-Dimensional Nanofabrication by Block Copolymer Self-Assembly. *Adv. Mater.* **2014**, *26*, 4386−4396.

(11) Wan, L.; Ruiz, R.; Gao, H.; Albrecht, T. R. Self-Registered Self-Assembly of Block Copolymers. *ACS Nano*, **2017**, *11*, 7666−7673.

(12) Hur, Y. H.; Song, S. W.; Kim, J. M.; Park, W. I.; Kim, K. H.; Kim, Y.; Jung, Y. S. Thermodynamic and Kinetic Tuning of Block Copolymer Based on Random Copolymerization for High-Quality Sub-6 nm Pattern Formation. *Adv. Funct. Mater.* **2018**, *28*, 1800765.

(13) Gotrik, K. W.; Hannon, A. F.; Son, J. G.; Keller, B.; Alexander-Katz, A.; Ross, C. A. Morphology Control in Block Copolymer Films Using Mixed Solvent Vapors. *ACS Nano* **2012**, *6*, 8052−8059.

(14) Bai, W.; Hannon, A. F.; Gotrik, K. W.; Choi, H. K.; Aissou, K.; Liontos, G.; Ntetsikas, K.; Alexander-Katz, A.; Avgeropoulos, A.; Ross, C. A. Thin Film Morphologies of Bulk-Gyroid Polystyrene-*block*-polydimethylsiloxane under Solvent Vapor Annealing. *Macromolecules* **2014**, *47*, 6000−6008.

(15) Chavis, M. A.; Smilgies, D.-M.; Wiesner, U. B.; Ober, C. K. Widely Tunable Morphologies in Block Copolymer Thin Films Through Solvent Vapor Annealing Using Mixtures of Selective Solvents. *Adv. Funct. Mater.* **2015**, *25*, 3057−3065.

(16) Bai, W.; Yager, K. G.; Ross, C. A. *In Situ* Characterization of the Self-Assembly of a Polystyrene−Polydimethylsiloxane Block Copolymer during Solvent Vapor Annealing. *Macromolecules* **2015**, *48*, 8574−8584.

(17) Lee, S.; Cheng, L.-C.; Gadelrab, K. R.; Ntetsikas, K.; Moschovas, D.; Yager, K. G.; Avgeropoulos, A.; Alexander-Katz, A.; Ross, C. A. Double-Layer Morphologies from a Silicon-Containing ABA Triblock Copolymer. *ACS Nano* **2018**, *12*, 6193−6202.

(18) Kao, J.; Thorkelsson, K.; Bai, P.; Zhang, Z.; Sun, C.; Xu, T. Rapid Fabrication of Hierarchically Structured Supramolecular Nanocomposite Thin Films in One Minute. *Nat. Commun.* **2014**, *5*, 4053.

(19) Albert, J. N. L.; Young, W.-S.; Lewis, III, R. L.; Bogart, T. D.; Smith, J. R.; Epps, III, T. H. Systematic Study on the Effect of Solvent Removal Rate on the Morphology of Solvent Vapor Annealed ABA Triblock Copolymer Thin Films. *ACS Nano* **2012**, *6*, 459−466.

(20) Gu, X.; Gunkel, I.; Hexemer, A.; Gu, W.; Russell, T. P. An In Situ Grazing Incidence X-Ray Scattering Study of Block Copolymer Thin Films During Solvent Vapor Annealing. *Adv. Mater.* **2014**, *26*, 273−281.

(21) Aissou, K.; Choi, H. K.; Nunns, A.; Manners, I.; Ross, C. A. Ordered Nanoscale Archimedean Tilings of a Templated 3- Miktoarm Star Terpolymer. *Nano Lett.* **2013**, *13*, 835−839.

(22) Xiong, S.; Wan, L.; Ishida, Y.; Chapuis, Y.-A.; Craig, G. S. W.; Ruiz, R.; Nealey, P. F. Directed Self-Assembly of Triblock Copolymer on Chemical Patterns for Sub-10-nm Nanofabrication *via* Solvent Annealing. *ACS Nano* **2016**, *10*, 7855−7865.

(23) Aissou, K.; Kwon, W.; Mumtaz, M.; Antoine, S.; Maret, M.; Portale, G.; Fleury, G.; Hadziioannou G. Archimedean Tilings and Hierarchical Lamellar Morphology Formed by Semicrystalline Miktoarm Star Terpolymer Thin Films. *ACS Nano* **2016**, *10*, 4055−4061.

(24) Aissou, K.; Mumtaz, M.; Marcasuzaa, P.; Brochon, C.; Cloutet, E.; Fleury, G.; Hadziioannou, G. Highly Ordered Nanoring Arrays Formed by Templated Si-Containing Triblock Terpolymer Thin Films. *Small* **2017**, *13*, 1603184.

(25) Berezkin, A. V.; Jung, F.; Posselt, D.; Smilgies, D.-M.; Papadakis, C. M. In Situ Tracking of Composition and Morphology of a Diblock Copolymer Film with GISAXS during Exchange of Solvent Vapors at Elevated Temperatures. *Adv. Funct. Mater.* **2018**, *28*, 1706226.

(26) Cheng, L.-C.; Gadelrab, K. R.; Kawamoto, K.; Yager, K. G.; Johnson, J. A.; Alexander-Katz, A.; Ross, C. A. Templated Self-Assembly of a PS-*Branch*-PDMS Bottlebrush Copolymer. *Nano Lett.* **2018**, *18*, 4360−4369.

(27) Stegelmeier, C.; Exner, A.; Hauschild, S.; Filiz, V.; Perlich, J.; Roth, S. V.; Abetz, V.; Förster, S. Evaporation-Induced Block Copolymer Self-Assembly into Membranes Studied by *in Situ* Synchrotron SAXS. *Macromolecules* **2015**, *48*, 1524−1530.

(28) Gu, Y.; Dorin, R. M.; Tan, K. W.; Smilgies, D.-M.; Wiesner, U. *In Situ* Study of Evaporation-Induced Surface Structure Evolution in Asymmetric Triblock Terpolymer Membranes. *Macromolecules* **2016**, *49*, 4195−4201.

(29) Weidman, M. C.; Smilgies, D.-M.; Tisdale, W. A. Kinetics of the Self-Assembly of Nanocrystal Superlattices Measured by Real-Time *In Situ* X-Ray Scattering. *Nat. Mater.* **2016**, *15*, 775−781.

(30) Lupi, F. F.; Giammaria, T. J.; Seguini, G.; Laus, M.; Dubček, P.; Pivac, B.; Bernstorff, S.; Perego, M. GISAXS Analysis of the In-Depth Morphology of Thick PS-*b*-PMMA Films. *ACS Appl. Mater. Interfaces* **2017**, *9*, 11054−11063.

(31) Lee, B; Park, I.; Yoon, J.; Park, S.; Kim, J.; Kim, K.-W.; Chang, T.; Ree, M. Structural Analysis of Block Copolymer Thin Films with Grazing Incidence Small-Angle X-Ray Scattering. *Macromolecules* **2005**, *38*, 4311−4323.

(32) Schappacher, M.; Deffieux, A. Synthesis of Macrocyclic Copolymer Brushes and Their Self-Assembly into Supramolecular Tubes. *Science* **2008**, *319*, 1512−1515.

(33) Ludwigs, S.; Böker, A.; Voronov, A.; Rehse, N.; Magerle, R.; Krausch, G. Self-Assembly of Functional Nanostructures from ABC Triblock Copolymers. *Nat. Mater.* **2003**, *2*, 744−747.

(34) Tang, P.; Qiu, F.; Zhang, H.; Yang, Y. Morphology and Phase Diagram of Complex Block Copolymers: ABC Linear Triblock Copolymers. *Phys. Rev. E* **2004**, *69*, 031803.

(35) Bang, J.; Kim, S. H.; Drockenmuller, E.; Misner, M. J.; Russell, T. P.; Hawker, C. J. Defect-Free Nanoporous Thin Films from ABC Triblock Copolymers. *J. Am. Chem. Soc.* **2006**, *128*, 7622−7629.

(36) Chuang, V. P.; Gwyther, J.; Mickiewicz, R. A.; Manners, I.; Ross, C. A. Templated Self-Assembly of Square Symmetry Arrays from an ABC Triblock Terpolymer. *Nano Lett.* **2009**, *9*, 4364−4369.

(37) Chang, A. B.; Bates, C. M.; Lee, B.; Garland, C. M.; Jones, S. C.; Spencer, R. K. W.; Matsen, M. W.; Grubbs, R. H. Manipulating the ABCs of Self-Assembly via Low-χ Block Polymer Design. *Proc. Natl. Acad. Sci. USA* **2017**, *114*, 6462−6467.

(38) Rodwogin, M. D.; Baruth, A.; Jackson, E. A.; Leighton, C.; Hillmyer, M. A. Nanoscale Rings from Silicon-Containing Triblock Terpolymers. *ACS Appl. Mater. Interfaces* **2012**, *4*, 3550−3557.

(39) Khanna, K.; Varshney, S.; Kakkar, A. Miktoarm Star Polymers: Advances in Synthesis, Self-Assembly, and Applications. *Polym. Chem.* **2010**, *1*, 1171−1185.

(40) Kawamoto, K.; Zhong, M.; Gadelrab, K. R.; Cheng, L.-C.; Ross, C. A.; Alexander-Katz, A.; Johnson, J. A. Graft-through Synthesis and Assembly of Janus Bottlebrush Polymers from A-*Branch*-B Diblock Macromonomers. *J. Am. Chem. Soc.* **2016**, *138*, 11501−11504.

(41) Lin, T.-P.; Chang, A. B.; Luo, S.-X.; Chen, H.-Y.; Lee, B.; Grubbs, R. H. Effects of Grafting Density on Block Polymer Self-Assembly: From Linear to Bottlebrush. *ACS Nano* **2017**, *11*, 11632−11641.

(42) Babayan, Y.; McMahon, J. M.; Li, S.; Gray, S. K.; Schatz, G. C.; Odom, T. W. Confining Standing Waves in Optical Corrals. *ACS Nano* **2009**, *3*, 615−620.

(43) Ren, Y.; Adeyeye, A. O.; Nam, C.; Ross, C. A. Effects of Interlayer Coupling in Elongated $Ni_{80}Fe_{20}$/Au/Co Nanorings. *IEEE Trans. Magn.* **2010**, *46*, 1906−1909.

(44) Li, K. H.; Ma, Z.; Choi, H. W. High-Q Whispering-Gallery Mode Lasing from Nanosphere-Patterned GaN Nanoring Arrays. *Appl. Phys. Lett.* **2011**, *98*, 071106.

(45) Chao, C.-C.; Wang, T.-C.; Ho, R.-M.; Georgopanos, P.; Avgeropoulos, A.; Thomas, E. L. Robust Block Copolymer Mask for Nanopatterning Polymer Films. *ACS Nano* **2010**, *4*, 2088−2094.

(46) Wu, N. L. Y.; Harris, K. D.; Buriak, J. M. Conversion of Bilayers of PS-*b*-PDMS Block Copolymer into Closely Packed, Aligned Silica Nanopatterns. *ACS Nano* **2013**, *7*, 5595−5606.

(47) Tu, K.-H.; Bai, W.; Liontos, G.; Ntetsikas, K.; Avgeropoulos, A.; Ross, C. A. Universal Pattern Transfer Methods for Metal Nanostructures by Block Copolymer Lithography. *Nanotechnology* **2015,** *26*, 375301.

(48) Zalusky, A. S.; Olayo-Valles, R.; Taylor, C. J.; Hillmyer, M. A. Mesoporous Polystyrene Monoliths. *J. Am. Chem. Soc.* **2001**, *123*, 1519−1520.

(49) Russell, T. P.; Hjelm, R. P., Jr.; Seeger, P. A. Temperature Dependence of the Interaction Parameter of Polystyrene and Poly(methyl methacrylate). *Macromolecules* **1990**, *23*, 890−893.

(50) Bosworth, J. K.; Black, C. T.; Ober, C. K. Selective Area Control of Self-Assembled Pattern Architecture Using a Lithographically Patternable Block Copolymer. *ACS Nano* **2009**, *3*, 1761−1766.

(51) Smilgies, D.-M. Scherrer Grain-Size Analysis Adapted to Grazing-Incidence Scattering with Area Detectors. *J. Appl. Cryst.* **2009**, *42*, 1030−1034.